

# Designing and discovering a new family of semiconducting quaternary Heusler compounds based on the 18-electron rule

Jiangang He,<sup>1</sup> S. Shahab Naghavi,<sup>2,1</sup> Vinay I. Hegde,<sup>1</sup> Maximilian Amsler,<sup>1,\*</sup> and Chris Wolverton<sup>1,†</sup>

<sup>1</sup>Department of Materials Science and Engineering, Northwestern University, Evanston, Illinois 60208, United States

<sup>2</sup>Department of Physical and Computational Chemistry,  
Shahid Beheshti University, G.C., Evin, 1983969411 Tehran, Iran

(Dated: February 6, 2022)

Intermetallic compounds with sizable band gaps are attractive for their unusual properties but rare. Here, we present a new family of stable semiconducting quaternary Heusler compounds, designed and discovered by means of high-throughput *ab initio* calculations based on the 18-electron rule. The 99 new semiconductors reported here adopt the ordered quaternary Heusler structure with the prototype of LiMgSnPd (F $\bar{4}3m$ , No. 216) and contain 18 valence electrons per formula unit. They are realized by filling the void in the half Heusler structure with a small and electropositive atom, i.e., lithium. These new stable quaternary Heusler semiconductors possess a range of band gaps from 0.3 to 2.5 eV, and exhibit some unusual properties different from conventional semiconductors, such as strong optical absorption, giant dielectric screening, and high Seebeck coefficient, which suggest these semiconductors have potential applications as photovoltaic and thermoelectric materials. While this study opens up avenues for further exploration of this novel class of semiconducting quaternary Heuslers, the design strategy used herein is broadly applicable across a potentially wide array of chemistries to discover new stable materials.

Heusler compounds are one of the largest families of ternary intermetallic compounds and have been intensely studied due to their simple crystal structure and broad range of applications [1–3]. The electronic structure and magnetic properties of Heusler compounds can be very well described by valence electron counting rules, i.e., the Slater-Pauling rule and 18-electron rule [3–6], enabling rational material design. Ternary Heusler compounds exist in three well-known varieties: full Heusler  $X_2YZ$  (FH); inverse Heusler  $XY_2Z$  (IH); and half Heusler  $XYZ$  (HH). In contrast to the intensively studied Ternary Heusler [3, 4, 7–11], quaternary Heusler  $XX'YZ$  compounds (QH) have not been as well explored yet, presumably due to the complexity of the quaternary phase space. As illustrated in Fig. 1, all these Heusler structures can be interpreted in terms of their relationship to the zinc blende  $XZ$  structure (space group F $\bar{4}3m$ , No. 216; Wyckoff positions:  $X$  (4a): (0, 0, 0) and  $Z$  (4c): (0.25, 0.25, 0.25); see Fig 1a), where both the octahedral  $4b$  (0.50, 0.50, 0.50) and tetrahedral  $4d$  (0.75, 0.75, 0.75) sites are unoccupied. HH  $XYZ$  is derived by filling the octahedral site (Wyckoff site  $4b$ ) in the zinc blende  $XZ$  structure with a  $Y$  atom (Fig 1b). Further filling the empty tetrahedral sites with another atom  $X'$  results in the QH  $XX'YZ$  structure (Fig 1c). FH  $X_2YZ$  is generated when  $X'$  and  $X$  are the same element, and subsequently its crystal symmetry increases to Fm $\bar{3}m$ , whereas IH  $XY_2Z$  is formed by substituting the  $X'$  atom with  $Y$  in the QH structure.

Most Heusler intermetallics have a metallic band structure and typically, only compounds with specific num-

bers of valence electrons can be semiconductors [3, 4, 12]. For instance, FH compounds containing 24 valence electrons per formula unit (f.u.) or HH compounds with 18 valence electrons per f.u. are likely to be semiconductors [3]. The band gap of these Heusler compounds is mainly determined by the magnitude of  $Y$ -site  $d$  orbital splitting in the crystal field and the hybridization between  $X$ -site  $d$ - and  $Z$ -site  $p$  orbitals [3, 5, 6, 13–15]. Many HH and FH semiconductors have been discovered and intensively studied for various applications such as thermoelectrics, transparent conductors, topological insulators, and buffer layers of solar cells [12, 13, 15–19]. Due to the plethora of exotic physical properties, the Heusler family has become a playground for the theoretical investigation of novel compounds. Recently, for instance, Gautier et al. systematically explored missing 18-electron  $XYZ$  ternary compounds by means of high-throughput (HT) *ab initio* virtual screening and discovered 20 new stable HH semiconductors with band gaps ranging from 1.5 eV to 3.0 eV from a dataset of 400 compounds [8, 13]. Many of these predicted compounds were subsequently synthesized experimentally—a powerful demonstration and validation of the HT computational approach.

Compared with the ternary Heusler (FH, HH, and IH) compounds, the quaternary phase space of the QH compounds affords a much higher freedom in tuning and designing electronic and magnetic structures for optical, electronics, and magnetic applications [20]. However, the number of the potential  $XX'YZ$  compounds is 3,265,290 ( $C_4^{73} \times 3$ ; 73 is the number of metallic elements [21], and there are 3 possible structures for each  $XX'YZ$  composition), which makes an exhaustive experimental search impractical. HT computation based on density functional theory (DFT) can screen this large phase space to identify promising candidates that are thermodynamically and dynamically stable, and in addition predict their ground

\* Current address: Laboratory of Atomic and Solid State Physics, Cornell University, Ithaca, New York 14853, USA

† c-wolverton@northwestern.edu

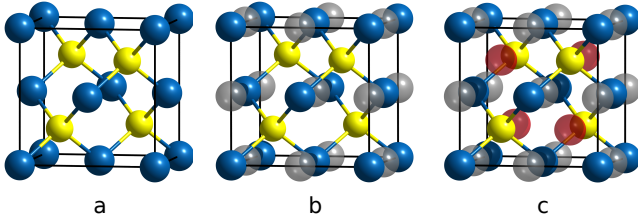


**Figure 1 — Comparison between zinc blende and Heusler structures.** **a.**  $XZ$  forms a zinc blende lattice. **b.** The half Heusler  $XYZ$  with  $Y$  occupying the octahedral void in the zinc blende lattice  $XZ$ . **c.** The quaternary Heusler  $XX'YZ$  with  $X'$  occupying the tetrahedral void of the half Heusler  $XYZ$ .  $X$ ,  $X'$ ,  $Y$ ,  $Z$  atoms are yellow, red, gray, and blue, respectively.

state crystal structure and interesting properties, thereby guiding and accelerating experimental efforts aimed at their successful synthesis [8, 10, 13, 22].

To search for new QH semiconductors efficiently, in this paper, we constrain our HT DFT screening to the Li-containing quaternary phase space (Li- $X$ - $Y$ - $Z$ ), including 53 possible elements in the  $X$ ,  $Y$ ,  $Z$  sites (elements with partially occupied  $f$  orbitals are excluded to avoid problems with convergence, see Supplementary for the full list), and considering compounds with 18 valence electron per f.u. The small atomic size of Li is very suitable for filling the void in a HH structure, and the electron donated by the electropositive Li can fully fill the valence band of the 17-electron HH  $XYZ$ . Hence, the corresponding 18-electron QH system obtained in this way is stabilized by fully filling bonding states, and accompanied by a band gap opening between the valence bonding states and the conduction anti-bonding states. Using HT DFT calculations within the framework of the Open Quantum Material Database (OQMD) [23, 24], and first-principles phonon calculations of 1320 candidate compounds, we find 99 Li-containing QH intermetallic semiconductors and 5 metals that are thermodynamically and dynamically stable. Based on our calculations, these compounds possess a wide range of band gaps (from 0.31 to 2.25 eV) with some candidates possessing exciting properties such as strong visible light absorption, giant high-frequency (electron) dielectric function, and high power factor. We hereby predict several promising candidates as energy harvesting materials for photovoltaic and thermoelectric applications.

## Design rules for semiconducting quaternary Heusler compounds

The emergence of a finite band gap in conventional semiconductors/insulators, such as Si, GaN, ZnS, and NaCl can be understood by the well-known octet rule [25, 26], where the fully occupied  $s$  and  $p$  orbitals form a  $s^2p^6$  closed shell. Owing to the close connection between the zinc blende (ZnS) and HH structure as mentioned before, the octet rule is also applicable to main-group-element-

based HH, such as LiMgAs and LiAlSi. Since transition metals have more low-lying energy states and  $d$  electrons, an 18-electron closed shell ( $s^2p^6d^{10}$ ) is required to open the band gap for a HH compound with one or two transition metal atoms; this is known as the 18-electron rule [8, 27]. The valence and conduction bands of HH, taking PtScGe as an example, are a consequence of the hybridization between Sc ( $Y$ -site)  $3d$  orbitals and Ge ( $Z$ -site)  $4p$  orbitals as depicted in Fig. 2c. Owing to the presence of a tetrahedral crystal field and the absence of inversion symmetry ( $T_d$  point group), the  $d$  orbitals of the transition metal atoms Pt and Sc split into  $T_2$  and  $E$  orbitals at the  $\Gamma$  point of the Brillouin zone, resulting in 10 orbitals,  $T_2$  (denoted as  $T_2^1$ ),  $E$  (denoted as  $E^1$ ),  $T_2$  (noted as  $T_2^2$ ), and  $E$  (noted as  $E^2$ ) from low to high energy. The band gap appears between the  $T_2^2$  and  $E^2$  orbitals that are mainly from Sc. The  $A_1$  band below the  $T_2^1$  stems from the  $4s$  orbital of the main group element Ge. Therefore, when the total valence electron count of the HH system is 18, the orbitals  $A_1$ ,  $T_2^1$ ,  $E^1$ , and  $T_2^2$  are fully occupied and the orbitals higher than the  $T_2^2$  are completely empty. As a consequence, the HH compound shows a semiconducting band structure. The size of the band gap mainly depends on the splitting between the  $T_2^2$  and  $E^2$  bands and the strength of hybridization between these orbitals. As expected, the 17-electron HH PtScGe is metallic with the Fermi level crossing the  $T_2^2$  band as demonstrated in Fig. 2c. A semiconducting state is achieved by filling the void in the HH  $XYZ$  compound with a fourth atom  $X'$  that possesses a suitable ionic radius, to minimize the strain, and a strong electropositivity, to donate its electron to other atoms thereby raising the Fermi level to the top of the valence band. Lithium is a good candidate to satisfy the above two conditions at the same time. As shown in Fig. 2e, the Li filled HH PtScGe, namely PtLiScGe, indeed has a band structure very similar to the corresponding 17-electron HH counterpart: the valence and conduction bands are mainly from Sc ( $Y$ -site)  $3d$  and Ge ( $Z$ -site)  $4p$  orbitals, respectively, whereas the Pt ( $Y$ -site)  $5d$  states are deeply buried below the Ge  $4p$  states. One  $2s$  electron from Li fills the empty portion of the valence band of PtScGe, resulting in a semiconductor with fully occupied valence bands and completely empty conduction bands. Owing to the high electropositivity, the Li atom donates its  $2s$  electron to the more electronegative atoms, i.e., Ge and Pt. The delocalization of Li  $2s$  can be clearly seen from the partial density of states (PDOS) shown in Fig. 2e.

Figs. 2f–g show the projected crystal orbital Hamilton populations (pCOHP) of PtScGe and PtLiScGe, which reflects the bonding interactions between various pairs of species in each compound. It is clear that Li–Ge and Li–Pt pairs have a strong bonding interaction below the Fermi level due to the charge transfer from Li to Ge and Pt, consistent with the large electronegativity difference between them. The bonding interactions between Pt and Ge do not change between the HH and QH except a downward shift with respect to Fermi level, whereas the

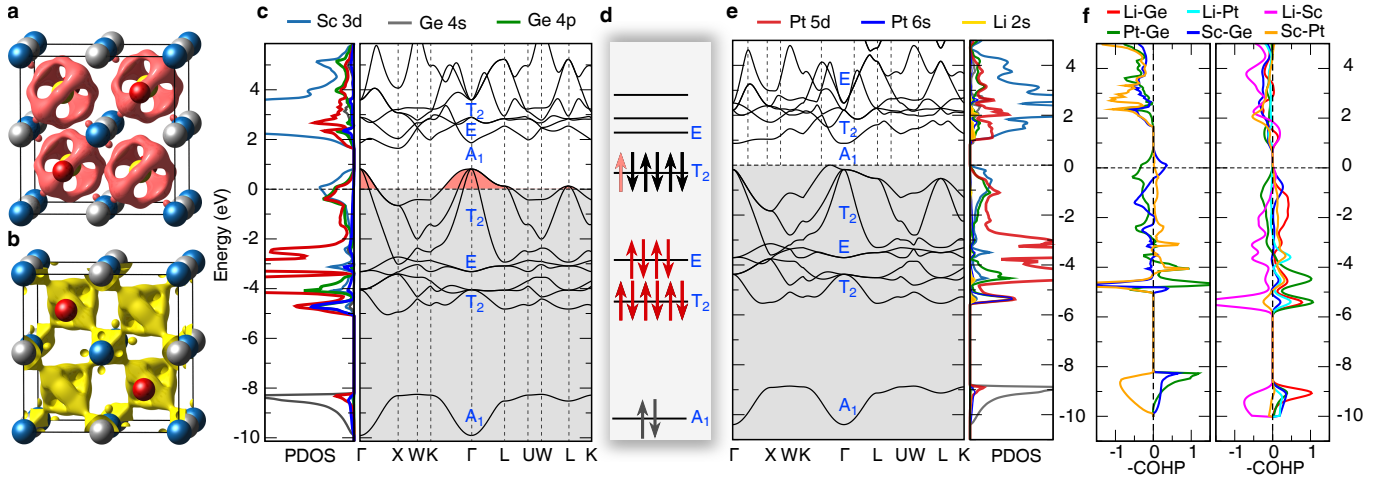


**Figure 2 | Electronic structure of a 17-electron half Heusler (PtScGe) vs. the corresponding 18-electron quaternary Heusler (PtLiScGe).** **a.** Charge density difference between PtLiScGe and PtScGe. **b.** Electron localization function (ELF) of PtLiScGe. **c.** band structure and partial density of states (PDOS) of PtScGe. **d.** band structure and PDOS of PtLiScGe. **e.** band structure and PDOS of PtLiScGe. **f.** crystal orbital Hamilton populations (-COHP) of PtScGe. **g.** -COHP of PtLiScGe.

anti-bonding interactions between Sc–Pt and Sc–Ge pairs are significantly reduced after inserting the Li atom. The main anti-bonding interaction in PtLiScGe is the Li–Sc pair, which are both strong electron donors, consistent with the fact that there are no stable Li–Sc binary compounds known.

## Thermodynamic stability and lattice dynamics

Thermodynamic stability is the most compelling and challenging criterion that has to be considered in predicting new compounds. In this paper, the thermodynamic stability is critically evaluated with respect to: (a) all the stable phases within the Li–X–Y–Z phase space, (b) chemical disorder within one rock-salt sublattice and between two rock-salt sublattices (see Supplementary for details), and (c) competing quaternary crystal structures for a given composition  $XLiYZ$ . Condition (a) was evaluated by constructing the convex hull of formation energies of all the competing compounds included in the OQMD [23, 24], which includes energetics of over 600,000 compounds, either reported in the Inorganic Crystal Structure Database (ICSD) or constructed from common binary and ternary prototype structures [21]. We find 99  $XLiYZ$  compounds to lie on the respective formation energy convex hull, implying that they are thermodynamically stable at zero Kelvin.

Since site occupancy disorder is commonly observed in Heusler compounds, the total energies of the 0 K stable QH phase were further compared with the disordered one simulated using special quasirandom structures (SQS) (see Supplementary for details). We find that ordered QH compounds always have much lower total energies than the corresponding disordered compounds (by  $\sim 100$  meV/atom; for scale, the ideal entropy of mix-

ing  $\Delta S_{\text{mix}} = \log_e 2 k_B$ , which is  $\sim 18$  meV at 300 K. See Supplementary Table S1 for details), indicating that most of the  $XLiYZ$  compounds are indeed ordered.

Nevertheless, the QH structure is not necessarily the ground state crystal structure of the  $XLiYZ$  composition as other structures might be lower in energy. To check whether other lower-energy crystal structures exist at a given  $XLiYZ$  composition, we performed global structure searches based on (a) Minima Hopping Method (MHM) as implemented in the Minihocao package [28, 29], and (b) particle-swarm optimization technique as implemented in the CALYPSO package [30, 31]. Since crystal structure prediction searches are computationally very expensive, around 10% QH compounds were randomly selected for these more refined searches. As tabulated in Supplementary Table S1, no other lower energy crystal structure was found for any of the selected QH compounds.

Furthermore, we examined the lattice dynamical stability of all the 99 QH compounds by performing phonon and elastic constant calculations (see the Methods section for details). The results show that all the newly discovered  $XLiYZ$  QH compounds are lattice dynamically stable. Therefore, we can safely claim that all  $XLiYZ$  compounds are thermodynamically and lattice dynamically stable in the ordered QH structure.

The distribution of the 99 Li-containing QH compounds in terms of chemistry is shown in Fig. 3. The site preference for different elements in these stable QH are uniform: Li and a late transition metal (Li–X) form one rock-salt sublattice, and an early transition metal and a main group element (Y–Z) form the other rock-salt sublattice. This elemental preference for an atomic site is very similar to a HH compound [8], where a vacancy and a late transition metal form one rock-salt sublattice. These findings are also consistent with our material de-



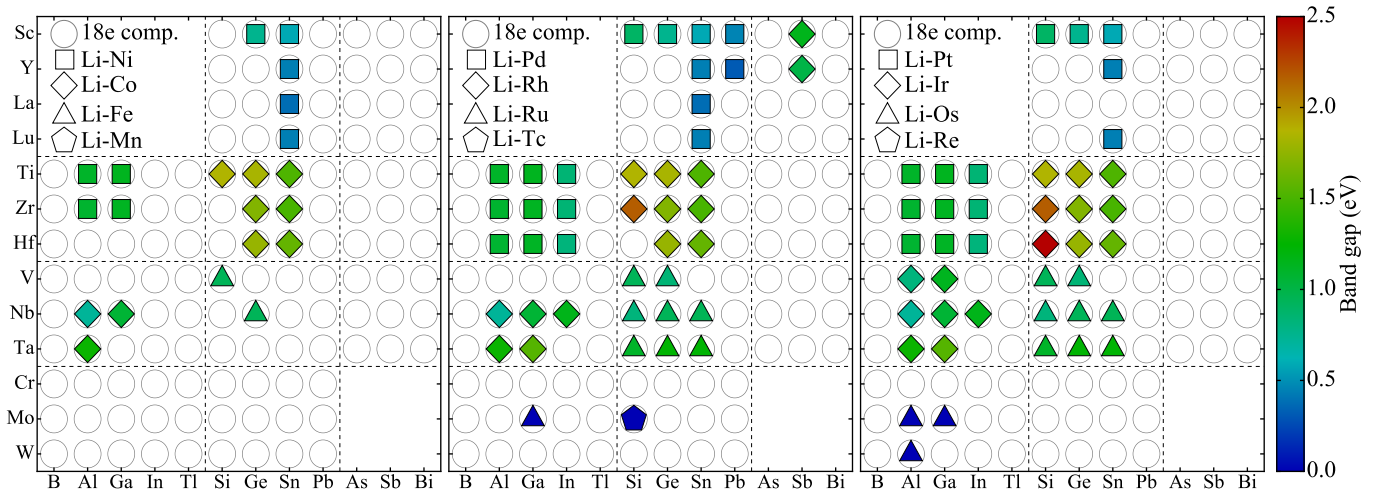


**Figure 3 | Heat map of band gap ( $E_g$ ) for stable Li-containing 18-electron QH compounds considered in this work.**  $XLiYZ$  compound is defined by the Li- $X$  and  $Y$ - $Z$  sublattices. Square, diamond, triangle, and pentagon shapes correspond to different Li- $X$  pairs with  $X$  = group 10, 9, 8, and 7 elements, respectively. Each circle represents an 18-electron compounds.

sign strategy, namely, the vacant site of a HH is filled with the Li atom which, on account of its electropositivity, readily bonds with the more electronegative late transition metal. Finally, the most stable QH compounds are mainly from the following groups,  $X$ : group 9 and 10;  $Y$ : group 3, 4, and 5;  $Z$ : group 13 and 14. The complete distribution of formation energy and convex hull distances for all the QH compounds studied in this paper are provided in the Supplementary Figs. S1 and S2.

## Electronic structure

After screening for thermodynamic and lattice dynamic stabilities, we calculated the band gaps of all the stable QH compounds using the screened hybrid functional HSE06 [32], since semilocal exchange-correlation functionals such as Perdew-Burke-Ernzerhof (PBE) [33] tend to underestimate band gaps. As shown in Fig. 3 all compounds are semiconductors with band gaps ranging from 0.3 to 2.5 eV except for Mo and W based QH (RuLiMoGa, OsLiMoAl, OsLiWAl, OsLiMoAl, and TcLiMoGa), which are metals. Among the semiconducting QH compounds, HfLiSiIr and PdLiYPb have the largest (2.5 eV) and smallest band gaps (0.3 eV), respectively. We see from Fig. 3 that the QH compounds containing elements from group 4 and 14 generally have larger band gaps than other compounds, and the metallic compounds are the ones containing a group 6 element. The magnitude of the band gap has a strong correlation with the electronegativity of  $X$ ,  $Y$ , and  $Z$ -site elements, and the  $d$  electron occupation of  $X$  and  $Y$  elements. All semiconductors have qualitatively similar band structure to PtLiScGe (Fig. 2e). Although Mo and W based QH are metals, the fundamental characteristics of their band structure are similar to that of PtLiScGe as well. The metallic nature is mainly a consequence of the weak hybridization between the  $X$  and  $Y$  elements due to a small difference in electroneg-

ativity. The electronic structure of our predicted QH compounds is quite different from conventional semiconductors, such as GaAs and ZnS, in that both the valence band and conduction bands are mainly from  $d$  orbitals. For all QH studied in this paper, the density of states around the Fermi level, which stems from the spatially localized  $d$  orbitals, is very high. It is therefore expected that these QH compounds have interesting applications as solar cells due to strong light absorption and thermoelectric materials because of the high thermopower, which will be discussed in the following two sections.

## Potential photovoltaic applications

Photovoltaic (PV) materials, which can directly convert sunlight into electric power, are one of the most important and promising renewable energy material platforms. The amount of sunlight absorbed directly limits the power conversion efficiency (PCE) of a solar cell. Since most solar radiation on the surface of the Earth is contained within 2 eV, high sunlight absorption in semiconducting PV material requires its band gap to be smaller than 2 eV. However, a high open-circle voltage ( $V_O$ ) demands a large band gap. For a single  $p$ - $n$  junction solar cell, the band gap of the PV material must be 1.2–2.0 eV to maximize PCE. In this paper we focus on the optical absorption properties and dielectric constants of the QH compounds with band gaps between 1.0 and 2.0 eV at the HSE06 level. The optical absorption coefficients ( $\alpha$ ) of such QH compounds containing earth-abundant elements were computed using the HSE06 functional (see Methods for details).

As shown in Fig. 4a, all QH compounds show very high  $\alpha$  in the visible light range, higher than other widely studied PV materials, such as  $\alpha$ -silicon, CdTe, CuInSe<sub>2</sub>, and CsSnI<sub>3</sub>. A strong interband optical absorption can be expected from the high joint density of state (JDOS) of

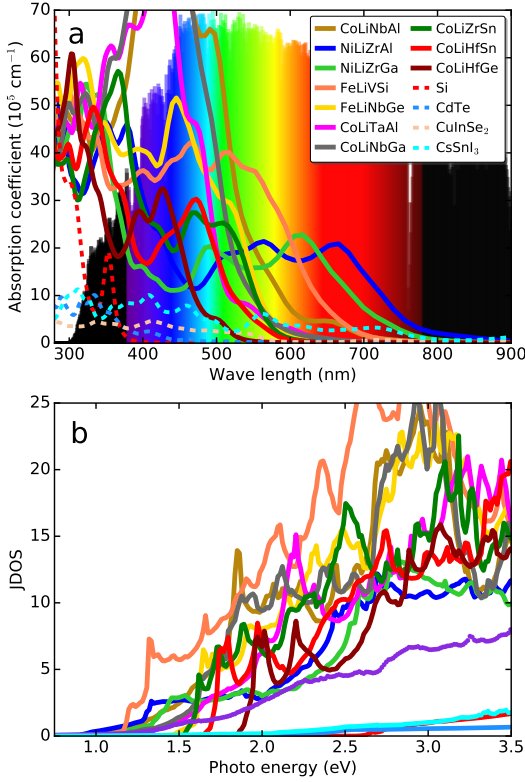


**Figure 4 — Optical properties of some selected quaternary Heusler compounds.** **a.** Optical absorption coefficients. **b.** joint density of states (JDOS) of the selected quaternary Heusler compounds, compared with conventional PV materials Si, CdTe, CuInSe<sub>2</sub>, and CsSnI<sub>3</sub>.

the QH compounds, in comparison to conventional PV materials (see Fig. 4b); this follows from the imaginary part of the dielectric function ( $\epsilon_2$ ) being proportional to the JDOS and the momentum transition matrix. The high JDOS of QH compounds is due to the fact that the states at the valence band maximum (VBM) and conduction band minimum (CBM) are mainly from the more localized  $d$  states of the transition metal atom as shown in Fig. 2d, and the  $d$ - $d$  transition is much stronger than the usual  $s$ - $p$  one. In contrast, the VBM and CBM of  $\alpha$ -silicon, GdTe, CuInSe<sub>2</sub>, and CsSnI<sub>3</sub> are from the more delocalized  $s$  and  $p$  orbitals. In addition, the restrictions imposed by dipole selection rules are alleviated by the broken inversion symmetry of the QH structure (F43m), which contributes to the large  $\alpha$  as well. Moreover, the structural similarity between QH and zinc blende makes QH a suitable buffer layer for semiconductors used in solar cells if their lattice constants match [17].

Other key factors required for high PCE materials are photo-generated electron-hole pair separation, carrier mobility, and carrier diffusion length, which are related to the exciton binding energy ( $E_{\text{bin}}$ ) and carrier effective masses ( $m^*$ ). In the Wannier-Mott (WM) model [34],  $E_{\text{bin}}$  is inversely proportional to the square of the high-frequency dielectric constant ( $\epsilon_\infty$ ) and proportional to the reduced effective mass ( $\mu$ ) of the electron ( $m_e^*$ ) and hole

**Table I — Electronic properties of quaternary Heuslers compounds suitable for PV applications.** Columns are band gap ( $E_g$ ), the minimal effective mass of electron ( $m_e$ ) and hole ( $m_h$ ), high-frequency dielectric constant ( $\epsilon_\infty$ ), and lattice constant ( $a$ ). The dielectric constants of QH are isotropic ( $\epsilon_\infty^{xx} = \epsilon_\infty^{yy} = \epsilon_\infty^{zz} = \epsilon_\infty$ ) due to the symmetry.

Compound	$E_g$ (eV)	$m_e$	$m_h$	$\epsilon_\infty$	$a$ (Å)
LiNbAlCo	1.041	0.404	0.314	24.2	5.963
LiZrAlNi	1.085	1.082	1.049	18.6	6.162
LiZrGaNi	1.150	1.408	0.812	18.0	6.124
LiVFeSi	1.191	0.881	0.929	24.0	5.615
LiNbFeGe	1.256	0.528	0.817	22.9	5.916
LiTaAlCo	1.460	1.145	0.349	21.2	5.944
LiNbGaCo	1.361	2.694	0.328	23.0	5.939
LiZrCoSn	1.486	2.405	1.407	18.4	6.300
LiHfCoSn	1.580	2.084	1.149	17.6	6.266
LiHfCoGe	1.755	1.001	1.067	16.3	6.016
LiTiCoSi	1.986	1.251	1.068	18.0	5.735
Si	1.190	1.315	0.401	11.2	5.437
CdTe	1.090	0.155	0.792	7.1	6.624
CuInSe <sub>2</sub>	0.620	0.176	1.097	8.7,	5.873,
				8.6	11.815
CsSnI <sub>3</sub>	0.840	0.285	0.179	7.7	6.119

( $m_h^*$ ) pair:  $E_{\text{bin}} \propto \frac{\mu}{\epsilon_\infty^2}$ . Therefore, large  $\epsilon_\infty$  and small  $\mu$  are favored for high PCE. Moreover, strong screening due to the large dielectric constant significantly reduces the probability of carrier trapping by impurities and defects, and electron-hole recombination. As listed in Table I, all QH semiconductors have very large values of  $\epsilon_\infty$ , 2–4 times larger than most well studied solar cell materials, such as Si, CdTe, CuInSe<sub>2</sub>, and CsSnI<sub>3</sub> computed at the same level of theory.

## Potential thermoelectric applications

Semiconducting Heusler (HH and FH) compounds have been widely studied as thermoelectric materials for converting waste heat into electricity. These Heusler compounds often possess a high power factor ( $\text{PF} = \sigma S^2$ ,  $\sigma$  and  $S$  are electrical conductivity and Seebeck coefficient, respectively) stemming from the high band degeneracy ( $N_v$ ), high density of states near the Fermi level, and the combination of “flat-and-dispersive” band structure [12, 35, 36]. However, the high intrinsic lattice thermal conductivity ( $\kappa_L \geq 10 \text{ Wm}^{-1}\text{K}^{-1}$  at 300 K) significantly impedes thermoelectric efficiency that requires a high PF and low overall thermal conductivity  $\kappa = \kappa_L + \kappa_e$ , where  $\kappa_e$  is the electron contribution. Therefore, semiconducting Heusler compounds with a high PF and low intrinsic  $\kappa_L$  are very promising candidate materials for thermoelectric applications [9, 12]. Here, we calculate  $\kappa_L$  of the newly discovered QH semiconductors with HSE06 band gaps  $E_g$  less than 1.2 eV by solving the linearized Boltzmann equation based on anharmonic third-order phonons with the ShengBTE package [37]. As shown in

Fig. 5, the calculated  $\kappa_L$  values for some of these compounds (LiScPdPb, LiYPdPb, LiYPdSn, LiScPtGe, and LiYPtSn) are around  $4\text{--}7\text{ Wm}^{-1}\text{K}^{-1}$  at 300 K, which are about two to four times lower than the widely studied HH thermoelectric materials, such as NiTiSn, computed at the same level of theory. We note that our calculated value of  $\kappa_L$  for NiTiSn agrees well with a previous calculation of  $16.8\text{ Wm}^{-1}\text{K}^{-1}$  at 300 K [9]. The computed  $\kappa_L$  values might be overestimated (e.g., NiTiSn: 13.5 and 9.3  $\text{Wm}^{-1}\text{K}^{-1}$  for calculation and experiment at 300 K, respectively) since our calculations neither include higher order force constants nor consider effects of defects and grain boundaries which can further scatter heat carrying phonons. We also compute the PF by solving the electronic Boltzmann equation with the constant relaxation time approximation, as implemented in the Boltztrap code [38] (see [Methods](#) for computational details). Similar to the well-studied half Heusler NiTiSn, all the QH compounds studied in this paper have reasonably high PF for both electron and hole transport assuming the same electron relaxation time ( $\tau = 15\text{ fs}$ ) as NiTiSn. The high power factor is due to (a) conduction band minimum (CBM) and valence band maximum (VBM) always being at low symmetry points of the Brillouin zone, resulting in a high valley-degeneracy, and (b) high density of states near the Fermi level at the top of valence band and bottom of conduction band mainly from the  $d$  orbitals of a transition metal (Fig. 2). Based on the same relaxation time ( $\tau = 15\text{ fs}$ ), we also estimate the  $zT$  of these QH compounds using the calculated  $\kappa_L$  values and the electronic thermal conductivity ( $\kappa_e$ ). The estimated  $zT = \frac{S^2\sigma}{\kappa_e + \kappa_L}$  values for these QH semiconductors at 300 K are 2–4 times higher than NiTiSn, as shown in Fig. 6. Interestingly, from Fig. 6 we see that these QH can possibly be used as either  $n$ -type or  $p$ -type thermoelectric materials with appropriate doping. Similar to other Heusler compounds, the  $\kappa_L$  can be further reduced by grain boundaries, alloying, nano-scale second-phase particles, etc.

## Conclusions

By employing high throughput DFT screening combined with phase stability analysis within the Open Quantum Materials Database, we discover 99 new, stable, and ordered quaternary Heusler semiconductors. Our discovery of this large set of new stable compounds is based on the design principle of filling the voids of the half Heusler with another atom to obtain 18 valence electrons, which is itself a conceptual extension of creating a half Heusler from the zinc blende structure. The inserted atom that can fill the void in the half Heusler structure should possess small size and high electropositivity. This is in contrast to filling the void in the zinc blende structure to generate half Heusler compounds, where late transition metals are favorable as their nearly full  $d$  states can be filled easily. The electronic structure of the quaternary Heusler compounds are very similar to that of half

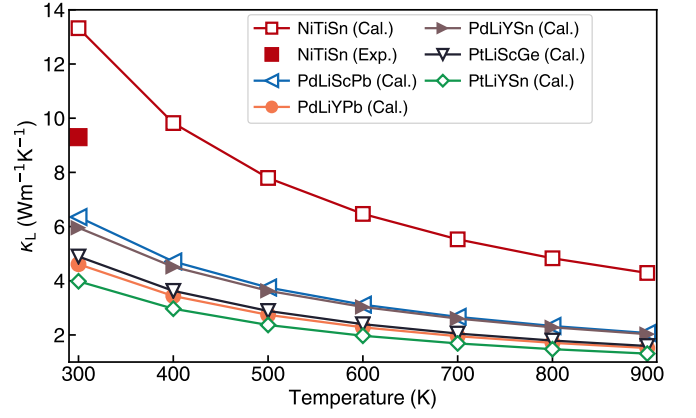


**Figure 5 — Lattice thermal conductivity.** The calculated (Cal.) lattice thermal conductivity of QH compound as function of temperature. The experimental (Exp.) and calculated (at the same level of theory) values of lattice thermal conductivity of NiTiSn are shown for reference.

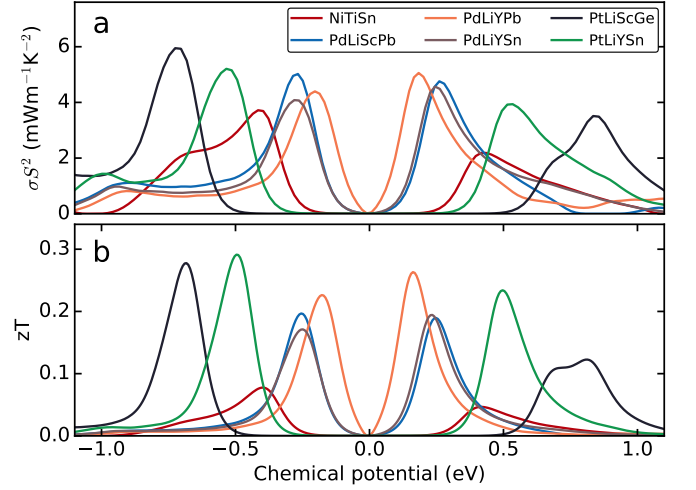


**Figure 6 — Calculated thermoelectric properties.** a. Power factor and b.  $zT$  as function of chemical potential at 300 K for QH, compared with that calculated for NiTiSn. A fixed relaxation time  $\tau = 15\text{ fs}$  was used for all the calculations.

Heusler compounds, where the valence and conduction bands are from the hybridization between  $X$ - $d$  and  $Z$ - $p$  orbitals, and the conditions of opening a band gap is the same: 18 valence electrons per formula unit are required to fully fill 9 valence bands.

Our initial studies on the properties of these QH compounds indicate that many of these semiconducting intermetallics have very high optical absorption in the visible light range and giant dielectric screening, which can significantly promote photogenerated electron-hole pair generation and separation, and therefore are attractive photovoltaic materials. Several QH semiconductors with smaller band gaps are found to possess the rare combination of simultaneous high power factor and low thermal conductivity, indicating promise for thermoelectric applications. Our discovery opens up possibilities for



synthesizing and designing novel materials for various applications in an accelerated fashion.

## Methods

All the HT calculations are based on DFT as implemented in Vienna Ab initio Simulation Package (VASP)[39, 40]. The Perdew-Burke-Ernzerhof (PBE) exchange-correlation functional [33] and plane wave basis set were used. The qmpy [23] framework was used for HT-DFT screening and phases from the Open Quantum Material Database (OQMD) [23] were used for convex hull construction. The lowest energy structure of  $XLiYZ$  was confirmed by using minima hopping crystal structure prediction method [28, 29] and particle-swarm optimization implemented in the CALYPSO package [30, 31] using a 16-atoms unit cell. Lattice dynamic stability was investigated by performing frozen phonon calculations using the phonopy package [41]. The site occupancy disorder in QH was investigated by comparing the energy of the ordered QH with the disordered QH simulated using special quasirandom structures (SQS).

The band gap, optical properties, and dielectric constants were computed by means of the screened hybrid functional HSE06 [32]. The high-frequency dielectric constant is calculated by using the perturbation expansion after discretization (PEAD) method [42, 43]. The absorption coefficient was calculated by using following formula

$$\alpha(\omega) = \frac{2\omega \sqrt{\frac{\epsilon_1^2(\omega) + \epsilon_2^2(\omega) - \epsilon_1(\omega)}{2}}}{c},$$

where  $\epsilon_1$  and  $\epsilon_2$  are the real and imaginary parts of dielectric function calculated at the HSE06 level, respectively,  $\omega$  is the photon frequency, and  $c$  is the speed of light.

Electron transport properties were calculated by using Boltztrap code within relaxation time approximation [38] with a  $41 \times 41 \times 41$   $\mathbf{k}$ -mesh. Electron thermal conductivity ( $\kappa_e$ ) is calculated from  $\sigma$ , using the Wiedemann-Franz law ( $\kappa_e = L_0 \sigma T$ ) with Lorenz number  $L_0 = 2.44 \times 10^{-8} \text{ W}\Omega\text{K}^{-2}$  [44]. Lattice thermal conductivities were calculated with the third-order phonon approach [45], with the linearized Boltzmann equation solved using the ShengBTE package [37]. The second and third-order interatomic force constants were calculated with a real-space supercell approach [41, 45]. The  $\kappa_L$  calculation was performed with a  $24 \times 24 \times 24$   $\mathbf{q}$ -mesh, see converge test in Supplementary Figs. S4.

## References

1. F. Heusler, *Deutsche Physikalische Gesellschaft* **5**, 219 (1903).
2. J. Dshemuchadse and W. Steurer, *Acta Crystallogr. A* **71**, 335 (2015).
3. T. Graf, C. Felser, and S. S. Parkin, *Prog. Solid State Chem.* **39**, 1 (2011).
4. I. Galanakis, P. H. Dederichs, and N. Papanikolaou, *Phys. Rev. B* **66**, 174429 (2002).
5. H. C. Kandpal, C. Felser, and R. Seshadri, *J. Phys. D: Appl. Phys.* **39**, 776 (2006).
6. C. Felser, *Heusler Alloys*, edited by C. Felser and A. Hirohata, Springer Series in Materials Science, Vol. 222 (Springer International Publishing, 2016) p. 492.
7. I. Galanakis, P. H. Dederichs, and N. Papanikolaou, *Phys. Rev. B* **66**, 134428 (2002).
8. R. Gautier, X. Zhang, L. Hu, L. Yu, Y. Lin, T. O. L. Sunde, D. Chon, K. R. Poeppelmeier, and A. Zunger, *Nat. Chem.* **7**, 308 (2015).
9. J. Carrete, W. Li, N. Mingo, S. Wang, and S. Curtarolo, *Phys. Rev. X* **4**, 011019 (2014).
10. S. Sanvito, C. Oses, J. Xue, A. Tiwari, M. Zic, T. Archer, P. Tozman, M. Venkatesan, M. Coey, and S. Curtarolo, *Sci. Adv.* **3**, e1602241 (2017).
11. J. Balluff, K. Diekmann, G. Reiss, and M. Meinert, *Phys. Rev. Materials* **1**, 034404 (2017).
12. J. He, M. Amsler, Y. Xia, S. S. Naghavi, V. I. Hegde, S. Hao, S. Goedecker, V. Ozoliņš, and C. Wolverton, *Phys. Rev. Lett.* **117**, 046602 (2016).
13. F. Yan, X. Zhang, Y. G. Yu, L. Yu, A. Nagaraja, T. O. Mason, and A. Zunger, *Nat. Commun.* **6**, 7308 (2015).
14. S. Chadov, X. Qi, J. Kübler, G. H. Fecher, C. Felser, and S. C. Zhang, *Nat. Mater.* **9**, 541 (2010).
15. W. G. Zeier, J. Schmitt, G. Hautier, U. Aydemir, Z. M. Gibbs, C. Felser, and G. J. Snyder, *Nat. Rev. Mater.* **1**, 16032 (2016).
16. T. Zhu, C. Fu, H. Xie, Y. Liu, and X. Zhao, *Adv. Energy Mater.* **5**, 1500588 (2015).
17. D. Kieven, R. Klenk, S. Naghavi, C. Felser, and T. Gruhn, *Phys. Rev. B* **81**, 075208 (2010).
18. M. Meinert, M. P. Geisler, J. Schmalhorst, U. Heinzmann, E. Arenholz, W. Hetaba, M. Stöger-Pollach, A. Hütten, and G. Reiss, *Phys. Rev. B* **90**, 085127 (2014).
19. D. I. Bilc, G. Hautier, D. Waroquiers, G.-M. Rignanese, and P. Ghosez, *Phys. Rev. Lett.* **114**, 136601 (2015).
20. L. Bainsla, A. I. Mallick, M. M. Raja, A. K. Nigam, B. S. D. C. S. Varaprasad, Y. K. Takahashi, A. Alam, K. G. Suresh, and K. Hono, *Phys. Rev. B* **91**, 104408 (2015).
21. S. Kirklin, J. E. Saal, V. I. Hegde, and C. Wolverton, *Acta Mater.* **102**, 125 (2016).
22. S. Curtarolo, G. L. Hart, M. B. Nardelli, N. Mingo, S. Sanvito, and O. Levy, *Nature mater.* **12**, 191 (2013).
23. J. E. Saal, S. Kirklin, M. Aykol, B. Meredig, and C. Wolverton, *JOM* **65**, 1501 (2013).
24. S. Kirklin, J. E. Saal, B. Meredig, A. Thompson, J. W. Doak, M. Aykol, S. Rühl, and C. Wolverton, *NPJ Comput. Mater.* **1**, 15010 (2015).
25. G. N. Lewis, *J. Am. Chem. Soc.* **38**, 762 (1916).
26. I. Langmuir, *J. Am. Chem. Soc.* **41**, 868 (1919).
27. D. M. P. Mingos, *J. Organomet. Chem.* **689**, 4420 (2004).
28. S. Goedecker, *J. Chem. Phys.* **120**, 9911 (2004).
29. M. Amsler and S. Goedecker, *J. Chem. Phys.* **133**, 224104 (2010).
30. Y. Wang, J. Lv, L. Zhu, and Y. Ma, *Phys. Rev. B* **82**, 094116 (2010).
31. Y. Wang, J. Lv, L. Zhu, and Y. Ma, *Comput. Phys. Commun.* **183**, 2063 (2012).
32. J. Heyd, G. E. Scuseria, and M. Ernzerhof, *J. Chem. Phys.* **118**, 8207 (2003), see also erratum, 124, 219906.

33. J. P. Perdew, K. Burke, and M. Ernzerhof, *Phys. Rev. Lett.* **77**, 3865 (1996).
34. N. W. Ashcroft and N. D. Mermin, *Solid State Physics* (Saunders College, Fort Worth, 1976).
35. D. I. Bilc, G. Hautier, D. Waroquier, G.-M. Rignanese, and P. Ghosez, *Phys. Rev. Lett.* **114**, 136601 (2015).
36. H. Xie, H. Wang, Y. Pei, C. Fu, X. Liu, G. J. Snyder, X. Zhao, and T. Zhu, *Adv. Funct. Mater.* **23**, 5123 (2013).
37. W. Li, J. Carrete, N. A. Katcho, and N. Mingo, *Comp. Phys. Commun.* **185**, 1747–1758 (2014).
38. G. K. Madsen and D. J. Singh, *Comput. Phys. Commun.* **175**, 67 (2006).
39. G. Kresse and J. Furthmüller, *Phys. Rev. B* **54**, 11169 (1996).
40. G. Kresse and J. Furthmüller, *Comput. Mater. Sci.* **6**, 15 (1996).
41. A. Togo and I. Tanaka, *Scr. Mater.* **108**, 1 (2015).
42. R. W. Nunes and X. Gonze, *Phys. Rev. B* **63**, 155107 (2001).
43. I. Souza, J. Íñiguez, and D. Vanderbilt, *Phys. Rev. Lett.* **89**, 117602 (2002).
44. R. Franz and G. Wiedemann, *Ann. der Phys. und Chemie* **165**, 497 (1853).
45. W. Li, L. Lindsay, D. A. Broido, D. A. Stewart, and N. Mingo, *Phys. Rev. B* **86**, 174307 (2012).

## Acknowledgments

J.H. (HT DFT, phonon, crystal structure search, optical and thermoelectric properties) and C.W. (conceived and designed the project) acknowledge support via ONR STTR N00014-13-P-1056. S.S.N. (optical and thermoelectric properties) was supported by US Department of Energy, Office of Science, Basic Energy Sciences, under grant DEFG02-07ER46433. V.H. (HT DFT) acknowledges support from the Department of Energy, under grant DE-SC0015106. M.A. (Minima Hopping) acknowledges

support from the Novartis Universität Basel Excellence Scholarship for Life Sciences, the Swiss National Science Foundation (P300P2-158407, P300P2-174475). This research was supported by resources from the National Energy Research Scientific Computing Center, a DOE Office of Science User Facility supported by the Office of Science of the U.S. Department of Energy under Contract No. DE-AC02-05CH11231, the Extreme Science and Engineering Discovery Environment (XSEDE) (which is supported by National Science Foundation Grant No. OCI-1053575), and the Quest high-performance computing facility at Northwestern University.

## Author contributions

The research was conceived and designed by J.H. and C.W. High throughput DFT calculations were carried out by J.H. and V.H. Photovoltaic, dielectric constant, and thermoelectric properties calculations were conducted by J.H. and S.S.N. Minima Hopping crystal structure searches were set up by M.A. Analysis of the data was performed by J.H. and S.S.N. Lattice thermal conductivity calculations were carried out by J.H., S.S.N., and M.A. All authors discussed the results contributed to writing the manuscript.

## Additional information

Supplementary information is available in the online version of the paper.

## Competing financial interests

The authors declare no competing financial interests.